



Synthesis of Porous g-C₃N₄ and Its Application as Photocatalyst for Methylene Blue Degradation

Grace Yuhaneka^{a,b}, Ade Irma Rozafia^a, Wahyu Prasetyo Utomo^{a,c}, Ani Iryani^d, Djoko Hartanto^{a,*}

^a Department of Chemistry, Faculty of Science and Data Analytics, Institut Teknologi Sepuluh Nopember (ITS), Sukolilo, Surabaya 60111, Indonesia; ^b Study Program of Laboratory Testing Analysis, SMK Negeri 1 Driyorejo, Gresik 61177, Indonesia; ^c School of Energy and Environment, City University of Hong Kong, Kowloon 999077, Hong Kong SAR; ^d Department of Chemistry, Faculty of Mathematics and Natural Sciences, Pakuan University, Bogor, Indonesia

Abstract Graphitic carbon nitride (g-C₃N₄) is a photocatalyst possessing a unique layered structure, remarkable thermal and chemical stability, and tunable bandgap. However, the bulk g-C₃N₄ has limited active sites and fast electron-holes recombination. In this work, we prepared porous g-C₃N₄ with an enhanced photoactivity toward methylene blue (MB) degradation. The porous g-C₃N₄ were prepared from melamine with addition of various amount of citric acid as a pore-forming agent (0.0 mmole, 0.1 mmole, 0.2 mmole, and 0.3 mmole; assigned as g-C₃N₄-0, g-C₃N₄-1, g-C₃N₄-2, and g-C₃N₄-3, respectively). The structural and morphological properties of the samples were analyzed using XRD, SEM, FTIR, and N₂ sorption. The optical property was analyzed using UV-vis diffuse reflectance and photoluminescence spectroscopy. Meanwhile the electronic conductivity was analyzed using Mott-Schottky analysis and electron impedance spectroscopy (EIS). The photocatalytic test revealed that g-C₃N₄-2 exhibited the highest MB degradation rate ($k = 0.00904 \text{ min}^{-1}$), while the bulk g-C₃N₄-0 showed the lowest rate ($k = 0.00689 \text{ min}^{-1}$). The g-C₃N₄-2 possessed relatively smaller crystallite size (~43.5 nm) and a larger surface area (13.975 m² g⁻¹) compared to the bulk g-C₃N₄-0 (crystallite size: 46.9 nm; surface area: 9.163 m² g⁻¹). The optical property and charge carrier transfer analysis also revealed that the g-C₃N₄-2 possessed more efficient charge carrier transfer, which suppress the charge recombination. The combination between a larger surface area and more efficient charge carrier transfer contributes to the enhanced photocatalytic activity of porous g-C₃N₄ toward MB degradation.

Keywords: carbon nitride, photocatalysis, photodegradation, dye, water treatment

*For correspondence:

djokohar@its.ac.id

Received: 7 Nov 2021

Accepted: 23 August 2022

© Copyright Yuhaneka.

This article is distributed under the terms of the [Creative Commons Attribution License](https://creativecommons.org/licenses/by/4.0/), which permits unrestricted use and redistribution provided that the original author and source are credited.

Introduction

Dye waste is considered as a hazardous waste, having negative impacts on the environment and human health [1]. Worldwide, around 7×10^5 metric tons of organic dye waste are discharged directly into water bodies, which have the potential to be a source of carcinogenic, teratogenic, and mutagenic materials in humans and other organisms [2-3]. Therefore, treatment of organic dyes in wastewater becomes significantly important. Several dye waste treatments have been developed, such as adsorption, chemical deposition, and filtration using membranes. Unfortunately, the afore mentioned treatments do not completely remove the existing dyes, rather they only transfer the dye molecules from water bodies to the other materials, i.e., the adsorbents, the sediments, or the membranes. Therefore, further

processing is still needed. Differently, the photodegradation treatment offers an interesting way to completely remove the dye from the wastewater. In the photodegradation process, the toxic dye molecules can be converted into less harmful ions or molecules or even completely decomposed into carbon dioxide (CO₂) and water (H₂O). Therefore, the photodegradation process becomes an attractive strategy for wastewater treatment [4].

Of the various types of semiconductor materials used for photocatalytic degradation, graphitic carbon nitride (g-C₃N₄) is considered as one of the most promising materials. g-C₃N₄ has a narrow bandgap (~2.7 eV), good chemical and thermal stability, practicality of mass production, and easy access to obtaining raw materials [5-7]. However, bulk g-C₃N₄ naturally has a low surface area (<10 m² g⁻¹) and a limited number of active sites [8], [9]. Additionally, the structure of g-C₃N₄, which is composed of bonded tri-s-triazine graphitic layer units, allows the delocalization of electron transfer. As a result, the recombination rate of the photogenerated carrier, i.e., hole (h⁺) and electron (e⁻), becomes very high [10-11]. The low surface area, limited active sites, and a high rate of electron-hole recombination rate together limit the photocatalytic activity of g-C₃N₄. Therefore, efforts to obtain g-C₃N₄ with a large surface area and improved charge separation efficiency are of great importance.

Some researchers have reported that the modification of the surface morphology of g-C₃N₄ by the formation of the pores can increase its surface area and photocatalytic activity. In this regards, some pore-forming agents could be used. For example, mesoporous g-C₃N₄ was successfully synthesized using melamine and carbonated beverages [7]. The sugar contained in the carbonated beverages was reported to serve as a pore-forming agent during the formation of g-C₃N₄. The evaluation of mesoporous g-C₃N₄ photocatalytic activity toward hydrogen evolution reaction (HER) showed that mesoporous g-C₃N₄ exhibited H₂ generation up to 15.1 times higher than bulk g-C₃N₄ due to its higher surface area, which provided a much higher amount of active site. A large number of pores in the g-C₃N₄ nanosheet also makes charge separation more efficient. Furthermore, porous g-C₃N₄ nanotubes were successfully synthesized from melamine with salicylic acid as a pore-forming agent. The porous g-C₃N₄ nanotubes had a large surface area and parallel channel structure. In this case, salicylic acid and its decomposition products facilitate the formation of g-C₃N₄ nanosheets. The formed nanosheet then rolls up and forms nanotubes. The porous nanotube structure ultimately showed a higher catalytic activity, which was about 6.7 and 2.4 times greater than bulk g-C₃N₄ for the 2-propanol decomposition reaction and CO₂ reduction. The improved photocatalytic activity was attributed to the higher surface area, more effective charge transfer, and the porous nanotube structure that made the diffusion of the reactants more efficient [12]. Recently, citric acid was also reported as an efficient pore-forming agent for preparing porous g-C₃N₄. The resulted porous g-C₃N₄ nanosheet possessed a higher surface area and pore volume, as well as the enhanced activity towards 2-propanol photodegradation. However, the addition of excess citric acid will cause the collapse of the g-C₃N₄ structure, thereby reducing its activity [9]. Therefore, the appropriate amount of the pore-forming agent is crucial to forming the porous g-C₃N₄ with the desirable properties. The afore mentioned reports clearly showed the superiority of the porous g-C₃N₄ compared to the bulky counterpart. However, the nature of the pore, e.g., pore volume and pore distribution, as well as the electronic conductivity, also influence the performance. The pore volume and size distribution may play a crucial role in determining the mass diffusion of the dye molecules to contact with the catalyst's active sites. Moreover, efficient electron transfer is also desirable for catalytic activity. Inspired by the recent development in the porous g-C₃N₄, herein we report the preparation and photocatalytic activity of porous g-C₃N₄ prepared from melamine and citric acid as a pore-forming agent and its performance toward methylene blue (MB) degradation. The use of citric acid could lead to the formation of a sheet-like structure and formed the pores in the g-C₃N₄ particles. Moreover, the prepared porous g-C₃N₄ has a more efficient electron transfer. The relatively higher surface area and the more efficient electron transfer finally contribute to the enhanced MB degradation under UV-LED irradiation.

Materials and methods

Materials. The materials used in this work are melamine (C₃N₃(NH₂)₃, Sigma-Aldrich, 99%), citric acid monohydrate (C₆H₈O₇·H₂O, Merck, ACS grade), methylene blue (C₁₆H₁₈ClN₃S, Merck), and deionized water.

Synthesis procedure. The synthesis of porous g-C₃N₄ was carried out with the addition of citric acid as reported by Kong et al. (2019). Initially, 2.52 g (0.02 mol) of melamine was dissolved into 40 mL of deionized water in 250 mL beaker glass. The mixture was then heated at 80 °C for 30 minutes under vigorous stirring using magnetic stirrer (700 rpm). Meanwhile, a stoichiometric amount of citric acid was dissolved in 10 mL of deionized water. Then, the citric acid solution was added dropwise into the melamine solution under stirring. The mixture of melamine and the citric acid solution was heated continuously for 2 hours at 80°C to produce a white suspension. The white suspension was then put into a 250 mL autoclave and heated in an oven at 180°C for 12 hours. After heating, the suspension was filtered and washed with deionized water several times. The filtered precipitate was then dried at 80 °C for 2 hours. The dried samples were then placed in a closed porcelain crucible and calcined in at a temperature of 550 °C for 2 hours. In this synthesis process, the amounts of citric acid were varied of 0.0 mmole, 0.1 mmole, 0.2 mmole, and 0.3 mmole. The obtained products were then assigned as g-C₃N₄-0, g-C₃N₄-1, g-C₃N₄-2, and g-C₃N₄-3, respectively [9].

Characterizations. The crystalline phase of the prepared samples was characterized by X-ray diffraction (XRD). The XRD analysis was performed using XRD PANalytical under Cu K α irradiation ($\lambda = 1.5406$), with accelerating voltage and current of 40 kV and 30 mA, respectively. The analysis was carried out at a diffraction angle of 2θ (20-80°) with a scan-interval of 0.017°. The average crystallite size was calculated based on the Scherer equation (Eq. 1).

$$D = \frac{0.89\lambda}{\beta \cos\theta} \quad (1)$$

where λ is the wavelength of X-ray, and β is the corrected full width at half maximum (FWHM). The Fourier-transformed infra-red (FTIR) was measured using Shimadzu IRAFFINITY-s using conventional KBr pellets. The surface morphology was observed using a scanning electron microscope (SEM) ZEISS EVO 10 with an accelerating voltage of 20 kV with a secondary electron (SE1) detector. The surface area was measured using Braneur-Emmet-Teller (BET) N₂ sorption. The optical properties were characterized by UV diffuse reflectance spectroscopy (DRS) using Shimadzu UV2600-I, in which BaSO₄ was used as the reference. The bandgap values were estimated by extrapolating the linear part of the plot $(F(R)h\nu)^{1/2}$ versus $h\nu$: $F(R)h\nu = A(h\nu - E_g)^2$, where $F(R) = (1-R)^2/2R$ stands for the Kubelka-Munk function calculated from the reflectance spectrum, and $h\nu$ is the photon energy (eV)(Li et al., 2016). The photoluminescence (PL) spectroscopy was performed using spectrofluorophotometer Shimadzu RF-5301 with an excitation wavelength of 350 nm. The Mott-Schottky plots were measured at a frequency of 0.5 kHz and amplitude of 0.01 V under ambient conditions. The electrochemical impedance spectroscopy (EIS) was performed at -0.2 V vs. Ag/AgCl at a frequency of 0.1 to 10⁵ Hz. Both Mott-Schottky and EIS analyses were performed using the CHI 600E instrument, where the g-C₃N₄ were prepared as a thin film prior to measurement.

Photocatalytic test. Photocatalytic activity of bulk g-C₃N₄ and porous g-C₃N₄ were evaluated using MB degradation under UV-LED irradiation ($\lambda = 365$ nm, 12 x 1 watt). Typically, 0.03 g of the photocatalyst was added to 30 mL of a 10 mg/L MB solution. Prior to the MB degradation test, the solution was allowed to stand for 1 hour under stirring in the dark to reach MB adsorption equilibrium. After 1 hour in the dark, the UV lamp was turned on. 2 mL of aliquot solution was taken periodically every 60 min up to 240 min. The concentration was determined using a UV-Vis spectrophotometer at a wavelength of 655 nm. The degradation rate constant was calculated based on the pseudo-first-order Langmuir-Hinselwood equation as shown in Eq. 2.

$$\ln \frac{C_t}{C_0} = kt \quad (2)$$

where C_t is the concentration at time t min (mg/L), C_0 is the initial concentration (mg/L), t is the reaction time (minutes), and k is the reaction rate constant [6].

Results and discussion

Structural and morphological properties. The XRD analysis was employed to investigate the phase structure of the samples [14]. As shown in Fig. 1, pronounce peaks were observed in all samples, which can be ascribed to the graphite phase $g\text{-C}_3\text{N}_4$. The peak at 2θ around 12.5° corresponds to the (100) crystal lattice of $g\text{-C}_3\text{N}_4$, which can be ascribed to the in-plane repetitive unit of tri-s-triazine. While the strongest peaks at around 27.5° refer to the (002) crystal plane, ascribing to the interplanar stacking peak of the conjugated aromatic rings [15]. Based on these XRD patterns, the $g\text{-C}_3\text{N}_4$ has been successfully formed with high purity. Even though the XRD patterns of the samples show a comparable feature, a more detail observation on the (002) planes show different FWHM values, which indicates the different crystallite size of the samples. The calculation of the crystallite size using the Scherer equation (Eq. 1) reveals that the porous $g\text{-C}_3\text{N}_4$ ($g\text{-C}_3\text{N}_4\text{-1}$, $g\text{-C}_3\text{N}_4\text{-2}$, and $g\text{-C}_3\text{N}_4\text{-3}$) posses lower crystallite size than that of bulk $g\text{-C}_3\text{N}_4$ ($g\text{-C}_3\text{N}_4\text{-0}$) as tabulated in Table 1. Considering the difference of the synthesis process between the bulk $g\text{-C}_3\text{N}_4$ and porous $g\text{-C}_3\text{N}_4$ was on the addition of the citric acid, we may speculate that the smaller crystallite size of the porous $g\text{-C}_3\text{N}_4$ was effected by the citric acid.

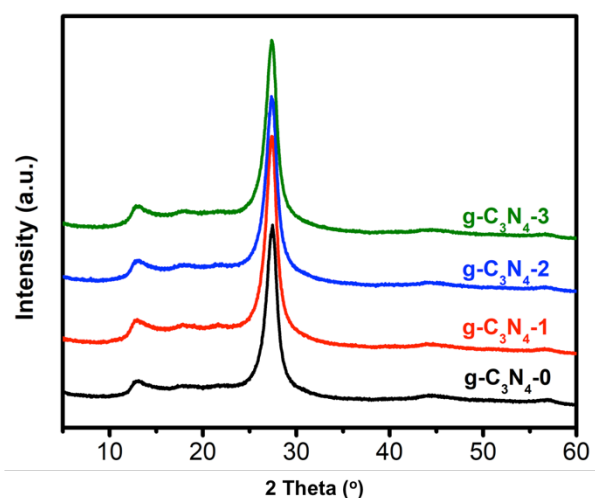


Fig. 1 XRD patterns of $g\text{-C}_3\text{N}_4$ -based photocatalysts.

Table 1 Crystallite size of $g\text{-C}_3\text{N}_4$ -based photocatalyst calculated from Scherer equation.

No	Samples	Crystallite size [nm]
1	$g\text{-C}_3\text{N}_4\text{-0}$	46.9
2	$g\text{-C}_3\text{N}_4\text{-1}$	46.1
3	$g\text{-C}_3\text{N}_4\text{-2}$	43.6
4	$g\text{-C}_3\text{N}_4\text{-3}$	43.8

The smaller crystallite size of porous $g\text{-C}_3\text{N}_4$ can be an indication of the pore formation during the calcination process due to the decomposition of citric acid. As reported by Kong et al. (2019), during the hydrothermal process, the citric acid was incorporated in the melamine precursor. During the calcination process in air atmosphere, the citric acid was decomposed to be CO_2 and H_2O , leaving pore in the $g\text{-C}_3\text{N}_4$ particles. The amount of the formed pores depends on the amount of the citric acid as a pore-forming agent. The more citric acid the more pores being formed. However, too much citric acid would lead to the destruction of the pore and particles. In this regard, the crystallite size can be an indication of the pore formation, since the more pore formed might lead to the smaller crystallite size [9]. This prediction was further supported by the surface area measurement. Using BET N_2 sorption method, the calculated surface area for bulk $g\text{-C}_3\text{N}_4\text{-0}$ and $g\text{-C}_3\text{N}_4\text{-2}$ (as a representative of porous $g\text{-C}_3\text{N}_4$) is 9.163

$\text{m}^2 \text{g}^{-1}$ and $13.975 \text{ m}^2 \text{g}^{-1}$, respectively. The increase in the surface area is attributed to the slightly higher amount of pores in the porous $\text{g-C}_3\text{N}_4$ [16]. This prediction is further verified by slightly increase of pore volume in $\text{g-C}_3\text{N}_4\text{-2}$ ($9.107 \times 10^{-2} \text{ mL}^3 \text{g}^{-1}$) compared to bulk $\text{g-C}_3\text{N}_4\text{-0}$, ($8.398 \times 10^{-2} \text{ mL}^3 \text{g}^{-1}$). Fig. 2 shows the SEM images of bulk $\text{g-C}_3\text{N}_4\text{-0}$ and porous $\text{g-C}_3\text{N}_4$. As presented in Fig. 2, all $\text{g-C}_3\text{N}_4$ samples have sheet-like structure. The effect of citric acid addition during $\text{g-C}_3\text{N}_4$ synthesis is exhibited by the presence of more holes or rough surface in the porous $\text{g-C}_3\text{N}_4$ compared to bulk $\text{g-C}_3\text{N}_4$. This result indicates the formation of pores during the synthesis process due to the decomposition of citric acid.

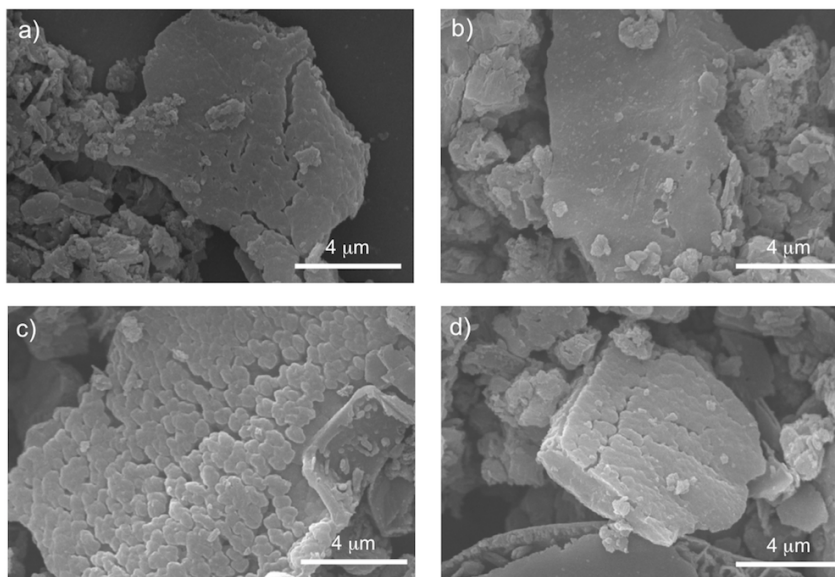


Fig. 2 SEM images of a) bulk $\text{g-C}_3\text{N}_4$, b) $\text{g-C}_3\text{N}_4\text{-1}$, c) $\text{g-C}_3\text{N}_4\text{-2}$, and d) $\text{g-C}_3\text{N}_4\text{-3}$.

To investigate the surface chemical structure of bulk $\text{g-C}_3\text{N}_4\text{-0}$ and porous $\text{g-C}_3\text{N}_4$, FTIR analysis was performed. Fig. 3 shows the FTIR spectra of all samples. All samples show a similar feature. A broad peak at 3140 cm^{-1} is attributed to the N–H bond stretching [17]. The peaks at 1234 , 1319 , 1404 , 1543 , and 1627 cm^{-1} can be ascribed to the vibration modes of the C–N stretching and C=N stretching in the aromatic ring [8]. Meanwhile, the peak at 810 cm^{-1} refers to the characteristic breathing vibration of the tri-s-triazine units ring in the framework [7], [18]. It is worthy to note that there is no additional peak in the porous $\text{g-C}_3\text{N}_4$, implying the full decomposition of citric acid [9].

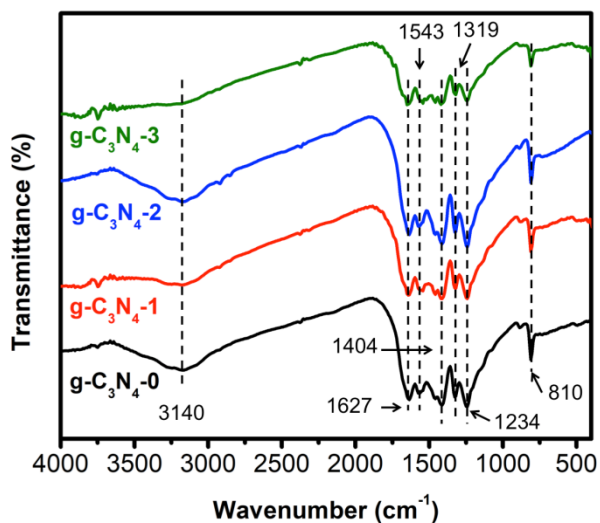


Fig. 3 FTIR spectra of $\text{g-C}_3\text{N}_4$ -based photocatalysts.

Optical properties. The UV-vis DRS analysis was used to investigate the optical absorption of the bulk $g\text{-C}_3\text{N}_4\text{-0}$ and porous $g\text{-C}_3\text{N}_4$. As shown in Fig. 4a, the DRS spectra of the samples show an almost comparable result. However, a slight absorption enhancement was observed in the visible region for the porous $g\text{-C}_3\text{N}_4$ compared to the bulk $g\text{-C}_3\text{N}_4$. The tailing edge of the porous $g\text{-C}_3\text{N}_4$ is slightly shifted to the lower energy (visible region) as presented in the Tauc plot (Fig. 4b). The calculated bandgap of the bulk $g\text{-C}_3\text{N}_4\text{-0}$ and porous $g\text{-C}_3\text{N}_4$ are 2.70 eV and ~ 2.68 eV, respectively, which is in good agreement with the previous report [18]. The UV-vis DRS results indicate that the porous structure in $g\text{-C}_3\text{N}_4$ does not significantly affect the absorption capacity of the samples or the bandgap.

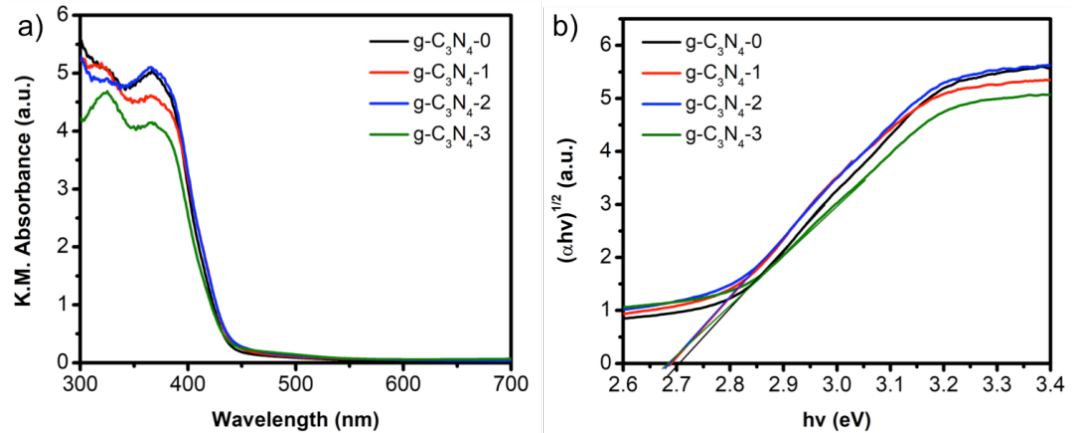


Fig. 4 a) DRS spectra and b) Tauc plots $g\text{-C}_3\text{N}_4$ -based photocatalysts.

The photophysical property of photogenerated carriers of bulk $g\text{-C}_3\text{N}_4\text{-0}$ and porous $g\text{-C}_3\text{N}_4$ were investigated using PL technique. As shown in Fig. 5, the PL emission peaks of all porous $g\text{-C}_3\text{N}_4$ clearly show lower intensity compared to the bulk $g\text{-C}_3\text{N}_4\text{-0}$, suggesting the suppressed recombination of the photogenerated charge carriers [19]. Among porous $g\text{-C}_3\text{N}_4$, the $g\text{-C}_3\text{N}_4\text{-2}$ shows the lowest PL peak intensity, which indicates that this sample has the highest suppression of charge carrier recombination. The suppression of the charge carrier recombination can be attributed to the presence of more pores and the smaller crystallite size of the porous $g\text{-C}_3\text{N}_4$ [9]. Due to presence of pores and smaller crystallite size, the photogenerated carriers (e^- and h^+) can easily reach the surface to contact with reactants, hence preventing the bulk charge recombination. These results suggest that the porous structure in $g\text{-C}_3\text{N}_4$ can significantly suppress the charge recombination.

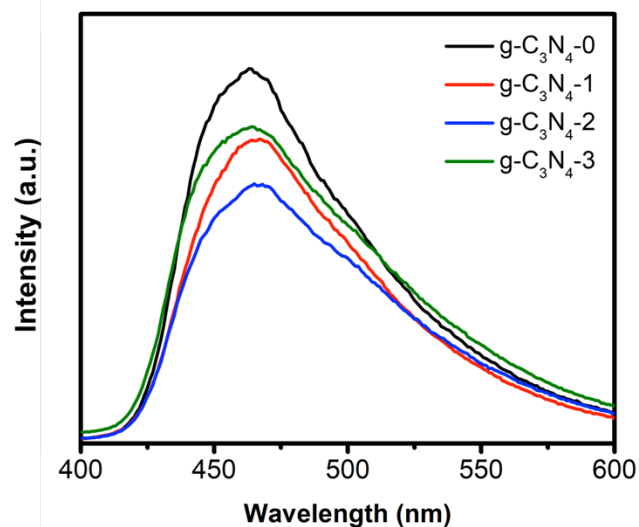


Fig. 5 PL spectra of $g\text{-C}_3\text{N}_4$ -based photocatalysts.

Charge carrier transfer property. The charge carrier transfer of bulk g-C₃N₄-0 and porous g-C₃N₄ was investigated by Mott-Schottky and EIS analysis. The electrochemical Mott-Schottky plots of bulk g-C₃N₄-0 and porous g-C₃N₄ show positive slopes, which represent the nature of n-type semiconductors. These results are in good agreement with the previous reports [15], [20], [21]. Moreover, the Mott-Schottky plots can be used to qualitatively determine the charge density of the materials. The charge carrier density can be calculated by Eq. 3.

$$Nd = \left(\frac{2}{e_0 \varepsilon \varepsilon_0} \right) \left[\frac{d \left(\frac{1}{C^2} \right)}{dV} \right]^{-1} \tag{3}$$

where e_0 is the electron charge, ε is the dielectric constant of g-C₃N₄, ε_0 is the permittivity of the vacuum, C is the differential capacity, V is the applied potentials at the electrode, and Nd is the carrier density. The charge density can be qualitatively compared since it is inversely proportional to the slope of the Mott-Schottky plots [22]. As can be seen in Fig. 6a, porous g-C₃N₄ generally exhibit lower slope than g-C₃N₄, suggesting higher charge carrier density than that of bulk g-C₃N₄-0. Furthermore, the EIS analysis was also performed to investigate the charge transfer resistance in g-C₃N₄-0 and porous g-C₃N₄. It is well known that the smaller arc radius indicates the smaller charge transfer resistance [23-25]. As shown in Fig. 6b, the porous g-C₃N₄ have smaller arc radii than that of bulk g-C₃N₄-0, suggesting the smaller charge transfer resistance in the porous g-C₃N₄. It is worth noting that g-C₃N₄-2 have the smallest slope of Mott-Schottky plots and the smallest arc radius of EIS spectra among all porous g-C₃N₄. Based on the Mott-Schottky and EIS analysis, the porous g-C₃N₄ have more efficient charge carrier transfer due to the higher carrier density and the smaller charge transfer resistance than bulk g-C₃N₄. Considering the similar bandgap values of the bulk and porous g-C₃N₄, the more efficient charge carrier transfer in porous g-C₃N₄ have a more significant role at determining the photocatalytic activity. In this regard, the bandgap energy determines the energy required for electronic excitation, which resulted in the formation of photogenerated charge carriers (e^- and h^+) [5]. Since all samples have the comparable bandgap values, so the opportunity of the charge carrier generation is the same. However, once the charge carriers were generated, the more efficient charge transfer from the bulk of g-C₃N₄ particles to the surface becomes the determining factor, where the most efficient charge transfer from the bulk to the surface will suppress the charge carrier recombination, hence enhancing the photocatalytic activity. Therefore, the more efficient charge carrier transfer in porous g-C₃N₄, especially g-C₃N₄-2, potentially enhances the photocatalytic activity since the charge carrier can easily reach the surface and contact the reactants. This result is also in a good agreement with the lowest charge recombination in PL spectra for g-C₃N₄-2 (Fig. 5).

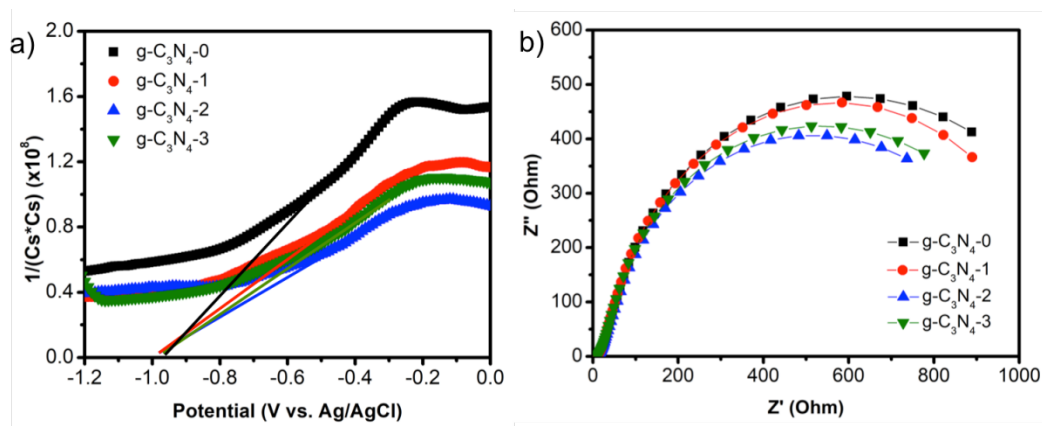


Fig. 6 a) Mott-Schottky plots and b) Nyquist plots of g-C₃N₄-based photocatalysts.

Photocatalytic activity. Photocatalytic activity of the prepared bulk g-C₃N₄-0 and porous g-C₃N₄ were evaluated by MB degradation under UV-LED irradiation. As presented in Fig. 7a, all samples are able to

degrade the MB molecules under UV LED irradiation. However, the MB degradation over porous g-C₃N₄ shows higher rate compared to the bulk g-C₃N₄. To compare to photocatalytic activity quantitatively, the MB degradation kinetics was further calculated using the Langmuir-Hinshelwood model (Eq. 2). Fig. 7b shows the pseudo-first-order kinetic plots of the MB degradation. As tabulated in Table 2, the porous g-C₃N₄ has higher reaction rate constant than that of bulk g-C₃N₄-0, indicating the positive effect of the porous structure in the g-C₃N₄. An obvious increase can be observed in the g-C₃N₄-2. Combining with the structural, morphological, optical, and charge carrier transfer analysis, the enhanced activity of MB photodegradation over porous g-C₃N₄ can be attributed to the relatively higher surface area and more efficient charge carrier transfer, which suppresses the charge recombination. The higher surface area increases the contact between the reactant molecules (either water or MB molecules) with the catalyst [26]. Hence, more molecules can be adsorbed on the catalyst surface. Furthermore, the more efficient charge carrier transfer in porous g-C₃N₄ suppress the charge carrier recombination and facilitated the electron migration from the bulk particles to the surface to further contact with the adsorbed molecules.

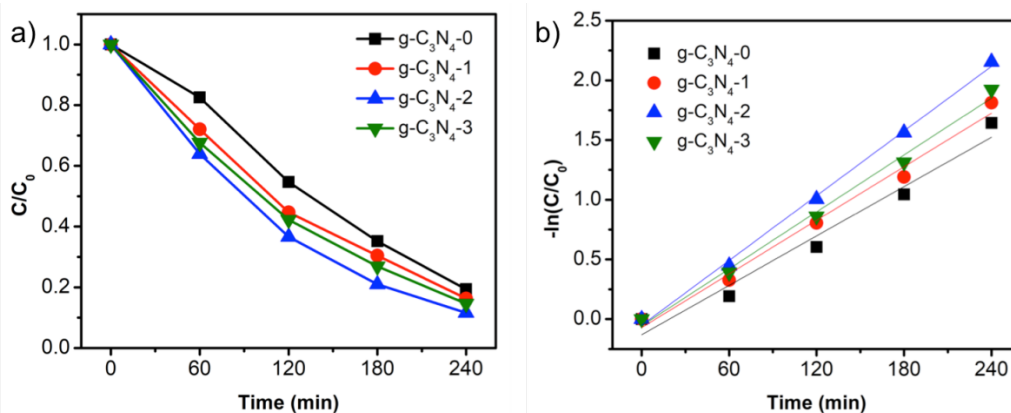


Fig. 7 a) MB photodegradation under UV-LED and b) Langmuir-Hinshelwood model fitting over g-C₃N₄-based photocatalysts.

Table 2 Rate constant of MB degradation over g-C₃N₄-based photocatalysts.

No	Samples	k [min ⁻¹]
1	g-C ₃ N ₄ -0	0.00689
2	g-C ₃ N ₄ -1	0.00749
3	g-C ₃ N ₄ -2	0.00904
4	g-C ₃ N ₄ -3	0.00795

Conclusions

The porous g-C₃N₄ was successfully prepared using citric acid as a pore-forming agent. The pore formation can be indicated by the smaller crystallite size of porous g-C₃N₄ as well as the higher surface area than that of bulk porous g-C₃N₄. The porous formation seems not to have a significant effect on the light absorption capacity and the bandgap. However, it has a significant effect on the charge transfer efficiency, as indicated by the PL, Mott-Schottky, and EIS analysis. The combination between the higher surface area and the more efficient charge transfer contribute to the enhanced photoactivity. The porous g-C₃N₄ shows a higher MB degradation rate compared to the bulk g-C₃N₄. Therefore, the porous structure in g-C₃N₄ prepared using citric acid as a pore-forming agent is beneficial for enhancing the photocatalytic activity. However, optimization may still be needed to further enhance the performance.

Acknowledgments

The authors greatly acknowledge The Ministry of Education, Culture, Research, and Technology of

Indonesia for funding this work under the scheme of Penelitian Tesis Magister (PPS-PTM) 2022 with contract number of 084/E5/PG.02.00.PT/2022. We also highly acknowledge and appreciate Prof. Yun Hau Ng of the Catalysis for Alternative and Renewable Energy (CARE) Laboratory, City University of Hong Kong and his team for their help with optical characterizations and charge carrier measurements

References

- [1] A. Buthiyappan, A. R. A. Aziz, and W. M. A. W. Daud, "Recent advances and prospects of catalytic advanced oxidation process in treating textile effluents," *Reviews in Chemical Engineering*, vol. 32, no. 1, pp. 1–47, 2016.
- [2] L. Hu *et al.*, *RSC Adv.*, vol. 6, no. 82, pp. 78595–78610, 2016.
- [3] A. Iryani *et al.*, "Enhanced Removal of Soluble and Insoluble Dyes over Hierarchical Zeolites: Effect of Synthesis Condition," *Inorganics*, vol. 8, no. 9, pp. 52, 2020.
- [4] D. Ayodhya and G. Veerabhadram, "A review on recent advances in photodegradation of dyes using doped and heterojunction based semiconductor metal sulfide nanostructures for environmental protection," *Materials Today Energy*, vol. 9, pp. 83–113, 2018.
- [5] W.-J. Ong, L.-L. Tan, Y. H. Ng, S.-T. Yong, and S.-P. Chai, "Graphitic Carbon Nitride (g-C₃N₄)-Based Photocatalysts for Artificial Photosynthesis and Environmental Remediation: Are We a Step Closer To Achieving Sustainability," *Chem. Rev.*, vol. 116, no. 12, pp. 7159–7329, 2016.
- [6] P. Lu *et al.*, "Novel CaCO₃/g-C₃N₄ composites with enhanced charge separation and photocatalytic activity," *Journal of Saudi Chemical Society*, vol. 23, no. 8, pp. 1109–1118, 2019.
- [7] S. Sun *et al.*, "Mesoporous graphitic carbon nitride (g-C₃N₄) nanosheets synthesized from carbonated beverage-reformed commercial melamine for enhanced photocatalytic hydrogen evolution," *Mater. Chem. Front.*, vol. 3, no. 4, pp. 597–605, 2019.
- [8] H. Li, Z. Liang, Q. Deng, and W. Hou, "Band structure engineering of polymeric carbon nitride with oxygen/carbon codoping for efficient charge separation and photocatalytic performance," *Journal of Colloid and Interface Science*, vol. 564, pp. 333–343, 2020.
- [9] L. Kong *et al.*, "Porous size dependent g-C₃N₄ for efficient photocatalysts: Regulation synthesizes and physical mechanism," *Materials Today Energy*, vol. 13, pp. 11–21, Sep. 2019.
- [10] N. Tian, H. Huang, X. Du, F. Dong, and Y. Zhang, "Rational nanostructure design of graphitic carbon nitride for photocatalytic applications," *J. Mater. Chem. A*, vol. 7, no. 19, pp. 11584–11612, 2019.
- [11] Q. Xu, B. Cheng, J. Yu, and G. Liu, "Making co-condensed amorphous carbon/g-C₃N₄ composites with improved visible-light photocatalytic H₂-production performance using Pt as cocatalyst," *Carbon*, vol. 118, pp. 241–249, 2017.
- [12] L. Jia *et al.*, "Large-Scale Preparation of g-C₃N₄ Porous Nanotubes with Enhanced Photocatalytic Activity by Using Salicylic Acid and Melamine," *Ind. Eng. Chem. Res.*, vol. 59, no. 3, pp. 1065–1072, 2020.
- [13] C. Li, Z. Sun, Y. Xue, G. Yao, and S. Zheng, "A facile synthesis of g-C₃N₄/TiO₂ hybrid photocatalysts by sol-gel method and its enhanced photodegradation towards methylene blue under visible light," *Advanced Powder Technology*, vol. 27, no. 2, pp. 330–337, 2016.
- [14] D. Hartanto, R. M. Iqbal, W. E. Shahbihi, E. Santoso, H. Fansuri, and A. Iryani, "Effect of H₂O/SiO₂ Molar Ratio on Direct Synthesis of ZSM-5 from Bangka's Kaolin Without Pretreatment," *Mal. J. Fund. Appl. Sci.*, vol. 13, no. 4, pp. 817–820, 2017.
- [15] J. Li, Y. Wang, X. Li, Q. Gao, and S. Zhang, "A facile synthesis of high-crystalline g-C₃N₄ nanosheets with closed self-assembly strategy for enhanced photocatalytic H₂ evolution," *Journal of Alloys and Compounds*, vol. 881, p. 160551, 2021.
- [16] D. Hartanto, R. Kurniawati, A. B. Pambudi, W. P. Utomo, W. L. Leaw, and H. Nur, "One-pot non-template synthesis of hierarchical ZSM-5 from kaolin source," *Solid State Sciences*, vol. 87, pp. 150–154, 2019.
- [17] Y. Jiang, Z. Lin, Y. Zhang, Y. Lai, D. Liang, and C. Yang, "Facile synthesis of porous C-doped C₃N₄: fast charge separation and enhanced photocatalytic hydrogen evolution," *New Journal Chemistry*, vol. 44, no. 41, pp. 17891–17898, 2020.
- [18] S. K. Lakhera, R. T. Pangal, H. Y. Hafeez, and B. Neppolian, "Oxygen-Functionalized and Ni+x (x=2, 3)-Coordinated Graphitic Carbon Nitride Nanosheets with Long-Life Deep-Trap States and their Direct Solar-Light-Driven Hydrogen Evolution Activity," *ChemSusChem*, vol. 12, no. 18, pp. 4293–4303, 2019.
- [19] Z. Yong *et al.*, "Synthesis, Characterization, and Photocatalytic Activity of g-C₃N₄/KTaO₃ Composites under Visible Light Irradiation," *Journal of Nanomaterials*, vol. 2015, p. e821986, 2015.
- [20] H.-J. Li, B.-W. Sun, L. Sui, D.-J. Qian, and M. Chen, "Preparation of water-dispersible porous g-C₃N₄ with improved photocatalytic activity by chemical oxidation," *Phys. Chem. Chem. Phys.*, vol. 17, no. 5, pp. 3309–3315, 2015.
- [21] F. Wei *et al.*, "Oxygen self-doped g-C₃N₄ with tunable electronic band structure for unprecedentedly enhanced photocatalytic performance," *Nanoscale*, vol. 10, no. 9, pp. 4515–4522, 2018.
- [22] H. Y. Chung *et al.*, "Oxygen-deficient bismuth tungstate and bismuth oxide composite photoanode with improved photostability," *Sci. Bull.*, vol. 63, no. 15, pp. 990–996, 2018.
- [23] K. Ao, Q. Wei, and W. A. Daoud, "MOF-Derived Sulfide-Based Electrocatalyst and Scaffold for Boosted

- Hydrogen Production," *ACS Appl. Mater. Interfaces*, vol. 12, no. 30, pp. 33595–33602, 2020.
- [24] J. Cheng *et al.*, "Facile synthesis of g-C₃N₄/BiVO₄ heterojunctions with enhanced visible light photocatalytic performance," *Ceramics International*, vol. 43, no. 1, Part A, pp. 301–307, 2017.
- [25] Y. Zhang *et al.*, "Bimetallic Mo–Co nanoparticles anchored on nitrogen-doped carbon for enhanced electrochemical nitrogen fixation," *J. Mater. Chem. A*, vol. 8, no. 18, pp. 9091–9098, 2020.
- [26] A. Iryani, M. M. Ilmi, and D. Hartanto, "Adsorption study of Congo Red Dye with ZSM-5 directly synthesized from bangka kaolin without organic template," *Mal. J. Fund. Appl. Sci.*, vol. 13, no. 4, pp. 832–839, 2017.